

Magnetic-flutter-induced pedestal plasma transport

J.D. Callen, C.C. Hegna

University of Wisconsin, Madison, WI 53706-1609 USA

E-mail: callen@engr.wisc.edu, <http://homepages.cae.wisc.edu/~callen>

A.J. Cole

Columbia University, New York, NY 10027 USA

Abstract. Plasma toroidal rotation can limit reconnection of externally applied resonant magnetic perturbation (RMP) fields $\delta\mathbf{B}$ on rational magnetic flux surfaces. Hence it causes the induced radial perturbations δB_ρ to be small there, thereby inhibiting magnetic island formation and stochasticity at the top of pedestals in high (H-mode) confinement tokamak plasmas. However, the δB_ρ s induced by RMPs increase away from rational surfaces and are shown to induce significant sinusoidal radial motion (flutter) of magnetic field lines with a radial extent that varies linearly with δB_ρ and inversely with distance from the rational surface because of the magnetic shear. This produces a radial electron thermal diffusivity that is $(1/2)(\delta B_\rho/B_0)^2$ times a kinetically-derived, electron-collision-induced, magnetic-shear-reduced, effective parallel electron thermal diffusivity in the absence of magnetic stochasticity. These low collisionality flutter-induced transport processes and thin magnetic island effects are shown to be highly peaked in the vicinity of rational surfaces at the top of low collisionality pedestals. However, the smaller but finite level of magnetic-flutter-induced electron heat transport midway between rational surfaces is the primary factor that determines the electron temperature difference between rational surfaces at the pedestal top. The magnetic-flutter-induced non-ambipolar electron density transport can be large enough to push the plasma toward an electron density transport root. Requiring ambipolar density transport is shown to determine the radial electric field, the plasma toroidal rotation (via radial force balance), a reduced electron thermal diffusivity and increased ambipolar density transport in the pedestal. At high collisionality the various flutter effects are less strongly peaked at rational surfaces and generally less significant. They are thus less likely to exhibit flutter-induced resonant behavior and transition toward an electron transport root. Magnetic-flutter-induced plasma transport processes provide a new paradigm for developing an understanding of how RMPs modify the pedestal structure to stabilize peeling-ballooning modes and thereby suppress edge localized modes in low collisionality tokamak H-mode plasmas.

1. Introduction

Control of ELMs with RMPs. Pioneering experiments [1]–[10] in DIII-D have used edge resonant magnetic perturbations (RMPs) in H-mode pedestals to stabilize peeling-ballooning (P-B) instabilities and thereby suppress edge localized modes (ELMs). How RMPs control ELMs is not presently understood. An initial hypothesis [2]–[5] was that multiple RMPs produce overlapping magnetic islands that cause magnetic stochasticity, which induces stochasticity-driven transport and reduces the pressure gradient in the edge, thereby stabilizing the P-B modes. And satisfaction of the Chirikov vacuum-island-overlap criterion from the separatrix in to a normalized radius of about 0.85 has been found to provide a useful empirical criterion [5] for the RMP field strength required for ELM suppression in low collisionality DIII-D plasmas.

Models of plasma transport induced by RMPs. Many magnetic-stochasticity-based theoretical models have been developed [11]–[16] for the RMP-induced increase in plasma transport throughout the plasma edge. However, the predicted level of stochasticity-driven transport induced at the RMP vacuum-island strength is often much larger than experimentally-inferred levels [3, 12]. Also, the different structure and responses to RMPs [4, 6, 8, 9, 10] in the near-separatrix region ($0.97 \lesssim \Psi_N \lesssim 1.0$ in which Ψ_N is the normalized poloidal magnetic flux) and pedestal top region ($0.92 \lesssim \Psi_N \lesssim 0.97$) suggests the dominant physics is different in these two regions. In the “laminar” [6, 8] near-separatrix region the Kolmogorov length is longer than the field line connection length to the divertor plates and both these lengths are larger than the electron collision length [3]. This indicates collisional parallel transport and its radial projection are likely to be more important than magnetic stochasticity there. Further, extended MHD calculations usually predict [17]–[23] that extant, mostly diamagnetic-flow-driven edge plasma toroidal flows limit “penetration” of RMP fields and thereby cause RMP-induced radial perturbations to be small on most pedestal rational ($q = m/n$) magnetic flux surfaces. Thus, toroidal flows inhibit but do not entirely eliminate magnetic reconnection, island formation and stochasticity, particularly near the pedestal top where P-B instability drives may be largest [4]. In this situation the magnetic field structure at the pedestal top [20, 22, 23] can be better characterized by radially separated chains of magnetic islands with sinusoidal radial magnetic flutter of field lines between them — see Fig. 1. Recently, a new, fundamentally different type of transport model has been introduced [24, 25] which calculates the plasma transport caused by magnetic flutter. Finally, it has been hypothesized recently [9], [10] that a critical RMP effect for suppression of ELMs is they induce a region slightly inward of the pedestal top which has high radial transport that blocks inward expansion of the pedestal top, thereby reducing the pressure gradient there and stabilizing P-B modes. This paper develops the theory of flutter-induced plasma transport [24, 25] at the pedestal top further by determining the radial electric field its non-ambipolar electron density flux induces and the resultant changes in RMP-induced pedestal plasma transport.

RMP effects on H-mode pedestals. Experimental studies [6, 7, 8] and interpretive

plasma transport analyses [24] in low collisionality pedestals [4] indicate that at the pedestal top, which is the region this paper will focus on, RMPs usually affect the electron temperature (T_e) profile more than the density (n_e) profile when ELMs are suppressed. In particular, when the safety factor q_{95} and collisionality are held roughly constant, the dominant RMP-induced effect there is that the T_e gradient scale length (and hence electron thermal diffusivity) increases roughly quadratically [24] with the RMP-inducing I-coil current. This observation is consistent with either the stochastic or the flutter transport model since both scale with the square of the strength of the magnetic perturbations. Also, the density gradient scale length (and hence density diffusivity) at the pedestal top increases about a factor of three less [24] with the square of the I-coil current and the toroidal plasma flow increases relatively abruptly there when ELMs are suppressed [4], [26], [27]. In addition, ELM suppression only occurs in limited q_{95} windows [4, 7]. The T_e gradient scale length at the pedestal top [7, 8] increases significantly in the q_{95} resonance windows while the n_e gradient scale length is affected less there. The q_{95} resonance behavior is less pronounced at higher collisionality. In the near-separatrix region the most significant effect induced by RMPs is a reduction in the density gradient which indicates an increase in density transport there [24] that depends much more weakly on q_{95} . This is often called “density pumpout.” In addition, the striated density and heat deposition profiles on divertor plates [6, 28] and soft X-ray imaging [29] provide evidence for the separatrix splitting introduced by the 3D RMP fields. However, these near-separatrix effects will not be addressed in this paper.

Magnetic-perturbation-induced plasma transport. The largest collision-induced plasma transport process in plasmas is electron heat conduction [30] along the total magnetic field $\mathbf{B} = \mathbf{B}_0 + \delta\mathbf{B}$ which produces a parallel electron heat flux $\mathbf{q}_{e\parallel} \equiv -(n_e\chi_{e\parallel}/B^2)\mathbf{B}\mathbf{B}\cdot\nabla T_e$. It is usually assumed that the parallel electron thermal diffusivity $\chi_{e\parallel}$ is so large that it forces $\mathbf{B}\cdot\nabla T_e$ and hence $\mathbf{q}_{e\parallel}$ to vanish along the total \mathbf{B} field lines except near rational surfaces — see Appendix A in [25]. In this fluid-based description, flutter-induced radial transport [31] is induced only in narrow (\sim mm for DIII-D pedestal top parameters [24, 25]) dissipative layers around rational surfaces [32, 33] or within magnetic islands [34], with no significant radial transport outside these regions. However, magnetic stochasticity [35] and irreversible kinetic-based electron-collision-induced magnetic flutter effects [24, 25] produce generic radial electron thermal diffusivities $\chi_e^{\delta B} \propto \chi_{e\parallel}^{\text{eff}}(\delta B_\rho/B_0)^2$. Since $\chi_{e\parallel}^{\text{eff}}$ can be very large ($\sim 10^7$ – 10^{10} $\text{m}^2\cdot\text{s}^{-1}$), very small radial magnetic perturbations $\delta B_\rho/B_0 \sim 10^{-5}$ – 3×10^{-4} can easily produce radial electron thermal diffusivities larger than the typical experimental levels [36] of $\chi_{e\text{exp}} \sim 1$ $\text{m}^2\cdot\text{s}^{-1}$ in H-mode pedestals. In contrast to the stochasticity-based transport models other papers have developed [11]–[16], this paper explores magnetic-flutter-induced [24, 25] transport effects between rational surfaces, primarily at the top of H-mode pedestals where flow-screening can cause stochasticity to be insignificant.

Non-ambipolar transport effects. Magnetic-flutter-induced plasma transport is dominantly an electron transport process. It is caused by the non-stochastic spatial magnetic flutter induced by flow-screened RMPs fields. The model’s initial studies

[24, 25] concentrated on the flutter-induced electron heat transport, which is the model’s largest transport effect. Using a procedure analogous to that developed in the later stochasticity model papers [13, 14, 15], this paper develops a model for the effects of the non-ambipolar flutter-induced electron and extant ion density transport fluxes, and the additional RMP-induced ambipolar density flux that results for the radial electric field required for ambipolar transport. In the absence of RMPs the magnetic configuration is nearly axisymmetric (superscript sym) and the radial electric field E_ρ is usually determined by extant non-ambipolar ion transport processes; hence in analogy to stellarator plasma transport studies [37], this E_ρ^{sym} can be called an “ion transport root.” Adding the flutter-induced non-ambipolar electron density flux pushes the pedestal plasma toward an “electron transport root” E_ρ^{flutt} that would occur if this non-ambipolar density transport was dominant and must be set to zero for ambipolarity. More generally, equating the extant ion and flutter-induced electron non-ambipolar density fluxes yields the E_ρ^{amb} required for net ambipolar density transport. This ambipolarity requirement is equivalent to satisfying the plasma toroidal torque balance [38, 39]. The flutter-induced increase in the radial electric field to E_ρ^{amb} reduces the effective flutter-induced radial electron density and thermal diffusivities, increases the co-current toroidal torque on the plasma and produces an additional net ambipolar density transport flux in the pedestal region of H-mode plasmas.

The magnetic flutter model of plasma transport is relatively new [24, 25]. And its key differences from stochastic magnetic field models [11]–[16] are not yet broadly understood. Thus, section 2 presents a new, graphical illustration of what is meant by magnetic flutter and discusses the basics of the magnetic-flutter-induced plasma transport model. The following section briefly summarizes the equations that describe the physically most relevant toroidal flutter model [25]. Section 4 discusses the limiting case where the flutter-induced non-ambipolar electron density flux is dominant and must vanish. In particular, it develops analytic-based flutter-induced electron thermal diffusivity and T_e profile predictions at the pedestal top between two adjacent rational surfaces that result when this flutter ambipolarity constraint and magnetic island effects are taken into account. The following section discusses the general situation where the flutter-induced effects are not so dominant that they warrant a flutter ambipolarity constraint. There the flutter-induced non-ambipolar electron density flux is equated to the extant non-ambipolar ion density flux to yield E_ρ^{amb} . The effects of this self-consistently-determined electric field on the effective flutter-induced electron density and thermal diffusivities, toroidal plasma rotation and net ambipolar density transport are also discussed there. The penultimate section discusses how the flutter-induced transport effects are somewhat different at higher electron collisionality. The final section summarizes the results presented in this paper and suggests future steps in the development and testing of the magnetic-flutter-induced transport model.

2. Physics of flutter-induced plasma transport

Distinguishing properties of the flutter model. There are two key attributes of the magnetic-flutter-induced plasma transport model that distinguish it from other models of plasma transport. First, the flutter model assumes that the plasma toroidal rotation is large enough to cause strong flow-screening [17]–[23] of the RMP-induced fields at their rational surfaces in the pedestal region. This causes RMPs to induce thin magnetic islands that do not overlap (see for example [20, 23] and Fig. 1 below) and hence do not produce any significant magnetic stochasticity at the pedestal top, except perhaps in narrow regions around X-points of the radially isolated chains of magnetic islands. However, in the regions between the island chains they produce magnetic flutter. This magnetic flutter in the pedestal plasma produces irreversible kinetic-based electron-collision-induced radial electron transport [24, 25]. Second, in low collisionality pedestals [4] this transport is highly peaked at the RMP rational surfaces and flattens the T_e profile there. However, since radial heat transport is a series process, the change in T_e between rational surfaces is determined primarily by the highest impedance (lowest diffusivity) to heat transport which occurs roughly midway between the RMP rational surfaces. These two distinguishing features of the flutter model are discussed in greater detail in the following paragraphs.

Radial motion of field lines. The total magnetic field $\mathbf{B} \equiv \mathbf{B}_0 + \delta\mathbf{B}$ will be assumed to be composed of an axisymmetric equilibrium $\mathbf{B}_0 \equiv \nabla\psi_p(\rho) \times \nabla[q(\rho)\theta - \zeta]$ for which $\mathbf{B}_0 \cdot \nabla\rho = 0$ plus 3D spatial perturbations $\delta\mathbf{B}$. Radial field line excursions induced by a small m/n sinusoidal radial magnetic perturbation $\nabla\rho \cdot \delta\mathbf{B} = \delta\hat{B}_{\rho m/n}(\rho) \cos(m\theta - n\zeta) = \delta\hat{B}_\rho \cos\alpha$ will be considered. Here, $\rho \equiv (\psi_t/\pi B_{t0})^{1/2}$ (m) is the toroidal-flux-based average radius of the axisymmetric \mathbf{B}_0 flux surface, θ and ζ are straight-field-line poloidal and toroidal angles, and $\alpha \equiv m\theta - n\zeta$ is an (approximately poloidal) helical angle perpendicular to \mathbf{B}_0 on a flux surface. Along the axisymmetric \mathbf{B}_0 magnetic field lines $\zeta = q(\rho)(\theta - \theta_0)$. Near the m/n rational surface where $q(\rho_{m/n}) \equiv m/n$, $q(\rho) \simeq m/n + xq'$, in which $x \equiv [q(\rho) - m/n]/q'(\rho) \simeq \rho - \rho_{m/n}$ is the radial distance from the rational surface and $\alpha \simeq -nxq'\theta$. Thus, along \mathbf{B}_0 field lines the radial perturbation can be written as $\nabla\rho \cdot \delta\mathbf{B} = \delta\hat{B}_\rho \cos\alpha = \delta\hat{B}_{\rho m/n}(\rho) \cos[k_\parallel(x)\ell]$ in which $\ell \equiv R_0q(\theta - \theta_0)$ is the distance along a \mathbf{B}_0 field line from an initial θ_0 . For notational simplicity, $\delta\hat{B}_\rho$ will often represent $\delta\hat{B}_{\rho m/n}$ in this paper. Here, $k_\parallel(x) \equiv k'_\parallel x$, $k'_\parallel \equiv -nq'/R_0q = -k_\theta/L_S$, $k_\theta \equiv nq/\rho$ and $L_S \equiv R_0q/\hat{s}$ is the magnetic shear length with shear parameter $\hat{s} \equiv \rho q'/q$. The radial and helical angle projections of the magnetic field line equation $d\mathbf{x}/d\ell = \mathbf{B}/B$ are $dx/d\ell \simeq (\delta\hat{B}_\rho/B_0) \cos\alpha$ and $d\alpha/d\ell \simeq \mathbf{B}_0 \cdot \nabla\alpha/B_0 = k'_\parallel x$. The ratio of these two equations yields a 2D equation for the radial motion of a field line: $dx^2/d\alpha = (2\delta\hat{B}_\rho/k'_\parallel B_0) \cos\alpha$. Integrating this equation over α and using $\alpha \simeq k'_\parallel x\ell$ yields an implicit equation for the radial distance of the field line from the m/n rational surface as one moves a distance ℓ along \mathbf{B}_0 :

$$x(\ell) = \left(x_0^2 + [2\delta\hat{B}_\rho(x)/k'_\parallel B_0] \sin(k'_\parallel x\ell) \right)^{1/2}. \quad (1)$$

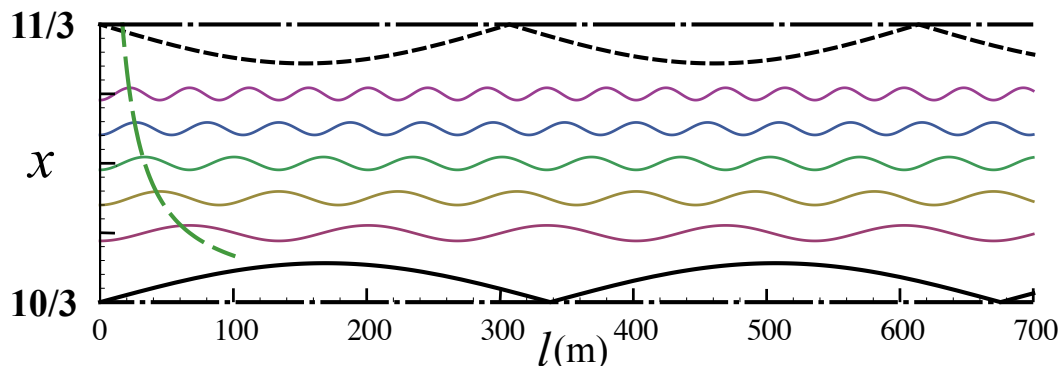


Figure 1. Radial fluttering of five $\mathbf{B}_0 + \delta\mathbf{B}$ magnetic field lines as they move a distance $\ell(\text{m})$ along \mathbf{B}_0 (horizontal coordinate). Here, the fluttering is induced by the RMP perturbation $\delta\hat{B}_{\rho 10/3}(x_0)$ between the 10/3 and 11/3 rational surfaces at which there are thin, isolated chains of magnetic islands. (For ease in visualization, the linearly-independent fluttering induced by the 11/3 perturbation in this same radial region is not shown.) The long dash (green) vertical curve indicates the radial variation of the magnetic-shear-induced periodicity length $1/|k'_{\parallel}x_0| = R_0q/|nx_0q'| = L_S/|k_{\theta}x_0|$ of the sinusoidal radial motion of the field lines. This length is typically much shorter than the electron collision length λ_e (~ 350 m for pedestal top parameters in Refs. [24, 25]).

Radially fluttering field lines: For an initial field line radial distance from a rational flux surface $x_0 \gg (2\delta\hat{B}_{\rho m/n}/|k'_{\parallel}B_0|)^{1/2} \equiv W/2\sqrt{2}$ [i.e., outside the assumed thin magnetic island of width W induced by $\delta\hat{B}_{\rho m/n}(0)$ at this rational surface], (1) can be approximated by

$$x(\ell) \simeq x_0 + \delta x(\ell), \quad (2)$$

in which the oscillatory radial excursion of a field line as one moves along \mathbf{B}_0 is

$$\delta x = \frac{\delta\hat{B}_{\rho m/n}(x_0)}{B_0} \frac{\sin[k'_{\parallel}x_0\ell]}{k'_{\parallel}x_0}. \quad (3)$$

Typical radial excursions (fluttering) of RMP-induced $\mathbf{B}_0 + \delta\mathbf{B}$ field lines between chains of thin, isolated magnetic island chains at two adjacent rational surfaces are shown in Fig. 1. The magnitude of the sinusoidal radial fluttering is approximately constant between these rational surfaces because while the δx in (3) is inversely proportional to x_0 it has been assumed here that the flow-screened $\delta\hat{B}_{\rho}(x_0)$ in the plasma increases almost linearly with x_0 in this region — see (20) below. Note that there is no magnetic stochasticity in Fig. 1. This is because flow-screening is assumed to reduce the RMP-induced $\delta\hat{B}_{\rho}$ at rational surfaces to small values where the thin magnetic islands they induce do not overlap and thus the Chirikov magnetic stochasticity criterion is not satisfied. Note also that this plot of radial field line motion is different from the usual Poincaré “puncture” plots which show the mapping of field lines on successive toroidal passes through a $\zeta = \text{constant}$ toroidal plane. Instead, Fig. 1 shows the continuous radial field line motion experienced by a charged particle as it moves a distance ℓ along a single \mathbf{B}_0 field line.

Flutter-induced radial diffusion. Neglecting drifts off flux surfaces, typical electrons stream along magnetic field lines with an electron thermal speed $v_{Te} \equiv \sqrt{2T_e/m_e}$ and are collisionally damped at a rate ν_e . For an electron collision length defined by $\lambda_e \equiv v_{Te}/\nu_e \simeq 1.3 \times 10^{16} [T_e(\text{eV})]^2 / [Z_{\text{eff}} n_e (\text{m}^{-3})]$ (m), which is longer than the magnetic-shear-induced sinusoidal periodicity length $1/|k'_{\parallel} x_0|$, radial excursions of electrons are limited to $\max\{\delta x\} \sim (1/|k'_{\parallel} x_0|) \delta \hat{B}_{\rho}(x_0)/B_0$. Using a phenomenological diffusivity $D \sim (\Delta x)^2/2\Delta t$ in which $\Delta x \simeq \max\{\delta x\}$ is the radial step taken in a time $\Delta t \sim 1/\nu_e$, the flutter-induced radial diffusivity induced by electron collisions is

$$D^{\text{flutt}} \sim \frac{\nu_e}{2(k'_{\parallel} x_0)^2} \left[\frac{\delta \hat{B}_{\rho}(x_0)}{B_0} \right]^2 \quad \text{for } |k'_{\parallel} x_0| \lambda_e > 1. \quad (4)$$

The radial distance off a rational surface where this result applies is

$$|x_0| > \delta_{\parallel} \equiv \frac{1}{|k'_{\parallel}| \lambda_e} = \frac{L_S \nu_e}{k_{\theta} v_{Te}}. \quad (5)$$

Magnetic shear causes the coefficient of the magnetic perturbations in D^{flutt} to decrease with distance x_0 from the rational surface as $1/x_0^2$. However, flow-screened radial magnetic perturbations $\delta \hat{B}_{\rho}(x_0)$ typically [18]–[23] grow approximately linearly with x_0 away from rational surfaces which tends to cancel the magnetic shear reduction effects to produce a small but finite electron diffusivity between rational surfaces.

Relation of T_e profile to thermal diffusivity profile. In the edge of H-mode plasmas the gradient of $T_e(\text{eV})$ is determined by [36, 40, 41, 42] the ratio of the radial conductive electron heat flow $P_{\text{cond}}(\text{W})$ per effective flux surface area $A \equiv V' \langle |\nabla \rho|^2 \rangle$ (m^2) to the density $n_e(\text{m}^{-3})$ times the radial electron thermal diffusivity $\chi_e(\text{m}^2 \cdot \text{s}^{-1})$: $-dT_e/d\rho = (P_{\text{cond}}/A)/(n_e \chi_e)$. Here, $V' \equiv dV(\rho)/d\rho$ in which $V(\rho)$ is the volume (m^3) of the ρ flux surface. In the thin dissipative singular layers ($x_0 \lesssim \delta_{\parallel} \sim \text{mm}$ for DIII-D pedestal top parameters in [4]) and/or magnetic islands ($x_0 < W/2$) around rational surfaces, the effective radial electron thermal diffusivity is very large [24, 25, 33], because x_0 is smallest there, which causes the gradient of T_e to be small there. However, the largest T_e gradients occur midway between rational surfaces where the flutter-induced χ_e is smallest [24, 25, 43]. Thus, the difference in T_e between rational surfaces is determined mainly by the smaller but finite χ_e between rational surfaces — see Figs. 2 and 3 below — because physically radial electron heat transport is a series process in which the lowest χ_e produces the largest impedance to radial electron heat flow.

3. Flutter-induced electron density and heat transport

Transport fluxes. Kinetic-based cylindrical and toroidal models of magnetic-flutter-induced radial electron density and heat transport have been developed [24, 25]. The most physically relevant toroidal model [25] uses a Lorentz collision model, accounts for parallel flows only being carried by untrapped (circulating) particles, resolves a collisional boundary layer in velocity space and includes effects of the near-separatrix toroidal geometry and finite inverse aspect ratio [$\epsilon \equiv (B_{\text{max}} - B_{\text{min}})/(B_{\text{max}} + B_{\text{min}}) \simeq 1/3$

in DIII-D]. The toroidal model [25] flutter-induced radial transport fluxes of electron density $\Gamma_{et}^{\text{flutt}} \equiv \langle \mathbf{\Gamma}_{et}^{\text{flutt}} \cdot \nabla \rho \rangle$ and heat $\Upsilon_{et}^{\text{flutt}} \equiv \langle \mathbf{q}_{et} \cdot \nabla \rho \rangle$ will be written in this paper as

$$\begin{bmatrix} \Gamma_{et}^{\text{flutt}} \\ \Upsilon_{et}^{\text{flutt}}/T_e \end{bmatrix} = -n_e \begin{bmatrix} D_{et} & D_T \\ \chi_n & \chi_{et} \end{bmatrix} \cdot \begin{bmatrix} d \ln \hat{p}_e / d\rho \\ d \ln T_e / d\rho \end{bmatrix}, \quad (6)$$

in which the relevant thermodynamic radial forces are proportional to

$$\frac{d \ln \hat{p}_e}{d\rho} = \frac{d \ln p_e}{d\rho} - \frac{e}{T_e} \frac{d\Phi_0}{d\rho}, \quad \frac{d \ln T_e}{d\rho} = \frac{1}{T_e} \frac{dT_e}{d\rho}. \quad (7)$$

The total magnetic-flutter-induced diffusivities are obtained by summing over all the m, n components:

$$\begin{aligned} \begin{bmatrix} D_{et} & D_T \\ \chi_n & \chi_{et} \end{bmatrix} &= \sum_{mn} \begin{bmatrix} D_{et}^{m/n} & D_T^{m/n} \\ \chi_n^{m/n} & \chi_{et}^{m/n} \end{bmatrix} \\ &\equiv \frac{v_{Te}^2}{\nu_e} \frac{1}{2} \sum_{mn} \left(\frac{\langle \delta \hat{B}_{\rho m/n}^{\text{pl}} \rangle}{B_{t0}} \right)^2 \begin{bmatrix} K_{00} & K_{01} \\ K_{10} & K_{11} \end{bmatrix}. \end{aligned} \quad (8)$$

The kinetically-derived Padé-approximate K_{ij} matrix of coefficients are defined by [25]

$$\begin{bmatrix} K_{00} & K_{01} \\ K_{10} & K_{11} \end{bmatrix} \equiv c_K \begin{bmatrix} G_{00} & G_{01} \\ G_{10} & G_{11} \end{bmatrix}, \quad (9)$$

in which the dimensionless coefficient is

$$c_K \equiv \frac{B_{t0}/B_{\text{max}}}{\langle v_{\parallel} |_{\lambda=1} / v \rangle} \frac{13}{24\pi}. \quad (10)$$

Here, the matrix $G_{ij}(x)$ of dimensionless, spatially-dependent geometric coefficients are

$$\begin{aligned} \begin{bmatrix} G_{00} & G_{01} \\ G_{10} & G_{11} \end{bmatrix} &\equiv \frac{4}{13 |X|^{3/2}} \left(\frac{|X|^{3/2}}{c_{\parallel t}} \int_0^{1/|X|^{1/2}} dy y^3 e^{-y} + \int_{y_{\text{min}}}^{\infty} dy e^{-y} \right) \\ &\times \begin{bmatrix} 1 & y - \frac{5}{2} \\ y - \frac{5}{2} & (y - \frac{5}{2})^2 \end{bmatrix}. \end{aligned} \quad (11)$$

Key parameters. Here, $p_e \equiv n_e T_e$ is the electron pressure and $\langle \delta \hat{B}_{\rho m/n}^{\text{pl}} \rangle$ is the “normal” [flux-surface-averaged (FSA) radial] m/n RMP fields induced in the plasma, which are to be provided by extended MHD codes that include flow-screening plasma response effects [17]–[23]. Further, B_{max} is the maximum magnetic field strength on the flux surface, $\langle v_{\parallel} |_{\lambda=1} \rangle \simeq (2v/\pi) \sqrt{1 - B_{\text{min}}/B_{\text{max}}}$ the FSA parallel untrapped electron speed at the trapped-untrapped boundary, $y_{\text{min}} \equiv \max\{1/|X|^{1/2}, 1/X_{\text{crit}}^{1/2}\}$ with $X_{\text{crit}} \equiv (2/3\sqrt{\pi}) (B_{t0}/B_{\text{max}}) (\lambda_e/R_0 q)$ being the low collisionality regime parameter, $c_{\parallel t} = (3/16) (B_{t0}^2/B_{\text{max}}^2) / (f_c \langle v_{\parallel} |_{\lambda=1} / v \rangle)$ with $f_c \equiv (3/4) (B_{t0}^2/B_{\text{max}}^2) \int_0^1 \lambda d\lambda / \langle \sqrt{1 - \lambda B/B_{\text{max}}} \rangle$ being the flow-weighted fraction of circulating particles, $y \equiv m_e v^2 / 2T_e$ the normalized electron energy and the normalized radial distance from the m/n rational surface is

$$X \equiv \frac{x}{\delta_{\parallel t}} = \frac{q(\rho) - m/n}{q' \delta_{\parallel t}} \simeq \frac{\rho - \rho_{m/n}}{\delta_{\parallel t}}. \quad (12)$$

Here, the relevant toroidal model [25] magnetic-shear-limited dissipative layer width is

$$\delta_{\parallel t} \equiv c_t \frac{L_S}{k_\theta \lambda_e}, \quad \text{with } c_t \equiv 3\sqrt{\pi} |\langle v_{\parallel} |_{\lambda=1} / v \rangle| \frac{B_{\max}}{B_{t0}}. \quad (13)$$

When ELMs are suppressed by RMPs in low collisionality DIII-D plasmas [4], typical pedestal top parameters at $\Psi_N \simeq 0.95$ ($\rho_N \equiv \rho/a \simeq 0.93$ with $a \simeq 0.79$ m) are [24, 25] $T_e \simeq 1130$ eV, $n_e \simeq 2.5 \times 10^{19} \text{ m}^{-3}$, $Z_{\text{eff}} \simeq 1.7$, $\lambda_e \simeq 350$ m, $v_{T_e}^2/\nu_e \simeq 7 \times 10^9 \text{ m}^2 \cdot \text{s}^{-1}$, $\langle \delta \hat{B}_{\rho m/n}^{\text{vac}} \rangle / B_{t0} \simeq 3.34 \times 10^{-4}$, $B_{\max}/B_{t0} \simeq 4/3$, $\langle v_{\parallel} |_{\lambda=1} / v \rangle \simeq 0.45$, $c_K \simeq 0.29$, $X_{\text{crit}} \simeq 17$, $c_{\parallel t} \simeq 0.94$, $c_t \simeq 3.2$ and $\delta_{\parallel t} \simeq 1.5$ mm.

Onsager symmetry. The normalized energy ($y \equiv m_e v^2 / 2T_e$) integrals in (11) produce a symmetric G_{ij} matrix. Thus, the flutter-induced diffusivity matrices in (8) are also symmetric. Hence, the flutter-induced electron transport fluxes are Onsager-symmetric in terms of the thermodynamic forces in (7).

Properties of G_{ij} . The G_{ij} matrix elements include [25] flutter-induced effects both near rational surfaces [first integral in (11), dominant at small $|X|$ and y] and asymptotically far from them [second integral in (11), dominant at large $|X|$ and y]. They are even functions of X . For $|X| \gg 1$ they decrease as $|x|^{-3/2}$, which indicates a slower decrease with increasing x than the x^{-2} decrease in the phenomenological D^{flutt} in (4) [24] — because of untrapped-particle collisional boundary layer effects [25]. The radial electron heat flux coefficient $|X|^{3/2} G_{11}$ becomes unity in the $|X| \rightarrow \infty$ limit when $X_{\text{crit}} \rightarrow \infty$ ($y_{\min} \rightarrow 1/|X|^{1/2}$). For small $|X|$, G_{11} is larger than unity. At the rational surface it becomes rather large: $\lim_{X \rightarrow 0} G_{11}(X) = 150/(13 c_{\parallel t})$.

Diffusivity ratios. All the $|X|^{3/2} G_{ij}$ coefficients except $|X|^{3/2} G_{11}$ are less than unity in the $|X| \rightarrow \infty$ limit. In this limit the ratio $G_{00}/G_{11} = 4/13$ for $X_{\text{crit}} \rightarrow \infty$. Thus, the ratio of the electron thermal to density “diagonal transport matrix element” diffusivities $\chi_{\text{et}}^{m/n}/D_{\text{et}}^{m/n}$ is about 3.25 in this limit, which is approximately applicable midway between rational surfaces. Also, whereas the ratio $D_T^{m/n}/D_{\text{et}}^{m/n}$ is $3/2$ near a rational surface, it is about $-3/2$ for $|x| \gg \delta_{\parallel t}$ (i.e., asymptotically far from rational surfaces), which applies to most of the region between rational surfaces. Since the coefficient of the $d \ln T_e / d\rho$ “electron thermal force” contribution to $\Gamma_{\text{et}}^{\text{flutt}}$ is negative ($\simeq -3/2$) in most of the region between rational surfaces, it reduces the electron density flux there. Similarly, the Onsager-symmetric “frictional heat flux” driven by $d \ln \hat{p}_e / d\rho$ reduces the flutter-induced conductive radial electron heat flux $\Upsilon_{\text{et}}^{\text{flutt}}$ between rational surfaces.

4. Predicted χ_e^{flutt} and T_e profiles with RMP ambipolarity constraint

Previous results. The initial flutter-induced transport papers [24, 25] estimated the radially-averaged effective electron thermal diffusivity $\bar{\chi}_e^{\text{flutt}}$ RMPs induce using the diagonal transport matrix diffusivity χ_{et} and a simple analytic model for $\langle \delta \hat{B}_{\rho m/n}^{\text{pl}}(x) \rangle$. While the estimates were larger than the $\chi_{e \text{ exp}}^{\text{sym}} \simeq 0.6 \text{ m}^2 \cdot \text{s}^{-1}$ values without RMPs, they were smaller than the experimentally-inferred RMP-induced values of $\chi_{e \text{ exp}}^{\text{RMP}} \sim 4 \text{ m}^2 \cdot \text{s}^{-1}$ at the top of DIII-D pedestals [24]. For more precise comparisons with DIII-D data, the off-diagonal transport matrix effects in (6) need to be taken into account and numerical

calculations of RMP-induced flow-screened radial magnetic perturbations in the plasma $\langle \delta \hat{B}_{\rho m/n}^{\text{pl}}(x) \rangle$ from extended MHD codes [17]–[23] need to be used.

Off-diagonal transport matrix effects. During the course of numerically evaluating [43] the flutter-induced electron transport model in (6)–(13) over many rational surfaces in the pedestal top region using $\langle \delta \hat{B}_{\rho m/n}^{\text{pl}}(x) \rangle$ profiles obtained from M3D-C1 [21, 23], two model extensions have been developed. The first is to go to the limit of imposing a “flutter ambipolarity constraint” by requiring that the radial electron density transport flux given by the first row of the matrix equation in (6) vanish so the flutter-induced electron transport does not produce a non-ambipolar flux:

$$\Gamma_{\text{et}}^{\text{flutt}} = -n_e \left(D_{\text{et}} \frac{d \ln \hat{p}_e}{d\rho} + D_T \frac{d \ln T_e}{d\rho} \right) \implies 0. \quad (14)$$

This flutter ambipolarity constraint yields

$$\frac{d \ln \hat{p}_e}{d\rho} \equiv \frac{d \ln p_e}{d\rho} - \frac{e}{T_e} \frac{d \Phi_0^{\text{flutt}}}{d\rho} = -\frac{D_T}{D_{\text{et}}} \frac{d \ln T_e}{d\rho}. \quad (15)$$

Taking account of this relation between the gradient scale lengths of \hat{p}_e and T_e in a radial electron heat flux $\Upsilon_{\text{et}}^{m/n} \equiv -n_e \chi_{\text{e eff}}^{m/n} dT_e/d\rho$ yields a modified, effective electron thermal diffusivity induced by the $\langle \delta \hat{B}_{\rho m/n}^{\text{pl}} \rangle$ -induced magnetic flutter:

$$\chi_{\text{e eff}}^{m/n} = \chi_{\text{et}}^{m/n} \left[1 + \left(\frac{\chi_n^{m/n}}{\chi_{\text{et}}^{m/n}} \right) \left(-\frac{D_T}{D_{\text{et}}} \right) \right] \simeq \frac{4}{13} \chi_{\text{et}}^{m/n}. \quad (16)$$

The approximate result at the end is applicable at the pedestal top outside narrow layers around the rational surfaces (i.e., for $|x| \gg \delta_{\parallel t} \simeq 1.5$ mm) where [25] $D_T/D_{\text{et}} \simeq D_T^{m/n}/D_{\text{et}}^{m/n} \simeq -3/2$ and $\chi_n^{m/n}/\chi_{\text{et}}^{m/n} \simeq (-3/2)/(13/4) = -6/13$.

Magnetic island effects. The second model extension is to estimate the possible effects of thin magnetic island chains at rational surfaces. Magnetic islands bifurcate the magnetic topology, because they produce closed 3D magnetic field structures in the plasma, as indicated in Fig. 1. They are created when a resonant magnetic perturbation reconnects magnetic field lines at a rational surface [$q(\rho_{m/n}) = m/n$] and causes the radial magnetic perturbation $\langle \delta \hat{B}_{\rho m/n}^{\text{pl}} \rangle$ to be nonzero there. The full width (across the O-point) of a m/n magnetic island is [44]–[46]

$$W \equiv 4 \left[L_S \langle \delta \hat{B}_{\rho m/n}^{\text{pl}}(0) \rangle / k_{\theta} B_{t0} \right]_{\rho_{m/n}}^{1/2}. \quad (17)$$

Magnetic islands effectively provide a radial short circuit for electron heat flow across the 3D island region [44] and reduce the global plasma energy confinement time $\propto W/a$ [44, 45]. Within the 3D island region the radial electron thermal diffusivity $\chi_{eW}^{m/n}$ is effectively infinite [44]. The flutter-induced plasma transport model is only valid [25] on field lines whose average distance $|x_0| \gg W/2\sqrt{2}$, as indicated before (2). The island O-point has a half width of $W/2$. Thus, outside the island region (i.e., for $|x_0| > W/2$) the flutter-induced $\chi_{\text{e eff}}^{m/n}$ is approximately applicable. For simplicity, in the transition between these regions the fraction of field lines that are outside the island will be approximated by the linear function $F_W^{m/n}(x) = (|x| - W/4)/(W/4)$. Hence, since $dT_e/d\rho \propto 1/\chi_e$, the effective radial electron thermal diffusivity in the vicinity of a

magnetic island at the m/n rational surface will be estimated by the reciprocal of the sum of the fractional inverses of the diffusivities inside and outside the island:

$$\chi_{eW\text{eff}}^{m/n} \simeq \left(\frac{1 - F_W^{m/n}(x)}{\chi_{eW}^{m/n}} + \frac{F_W^{m/n}(x)}{\chi_{e\text{eff}}^{m/n}(x)} \right)^{-1}, \quad (18)$$

in which the dimensionless spatial weighting function is

$$F_W^{m/n}(x) = \begin{cases} 0, & |x| < W/4, \\ \frac{|x| - W/4}{W/4}, & W/4 \leq |x| \leq W/2, \\ 1, & |x| > W/2. \end{cases} \quad (19)$$

In numerical evaluations [43] $\chi_{eW}^{m/n}$ only needs to be very large compared to $\chi_{\text{et}}^{m/n}(0)$.

Flow-screened RMP-induced field. The radial component of RMP-induced fields $\langle \delta \hat{B}_{\rho m/n}^{\text{pl}} \rangle$ in the plasma are reduced from their vacuum values $\langle \delta \hat{B}_{\rho m/n}^{\text{vac}} \rangle$ at rational surfaces by flow screening but grow approximately linearly away from them [17]–[23]. Motivated by the generic form of linear results from the MHD codes [18]–[23], they will be represented analytically in this paper for $|x| \lesssim L_{\delta B}$ by

$$\langle \delta \hat{B}_{\rho m/n}^{\text{pl}}(x) \rangle = \langle \delta \hat{B}_{\rho m/n}^{\text{vac}} \rangle \left(f_{\text{scr}}^2 + \frac{x^2}{L_{\delta B}^2} \right)^{1/2}, \quad (20)$$

in which the flow-screening factor is defined by

$$f_{\text{scr}} \equiv \frac{\delta \hat{B}_{\rho m/n}^{\text{pl}}(0)}{\delta \hat{B}_{\rho m/n}^{\text{vac}}(0)}. \quad (21)$$

Note that this f_{scr} factor, which is usually less than one on rational surfaces, is the inverse of that defined in [24, 25], to follow the convention introduced in [13].

Parameter choices. The flutter-induced electron thermal diffusivity and predicted T_e profile will be estimated analytically in the region between the 10/3 and 11/3 surfaces. Assume for these estimates that the flow-screening factor is $f_{\text{scr}} = 1/4$. Then, using DIII-D pedestal top parameters [24, 25] of $L_S \simeq 2.4$ m and $k_\theta \simeq 15$ m⁻¹, the estimated 10/3 and 11/3 island widths are $W \simeq 15$ mm. Since these island widths are less than the distance between these rational surfaces ($\simeq 1/nq' \simeq 28$ mm, which yields $X_{11/3} - X_{10/3} \simeq 1/\delta_{\parallel t} nq' \simeq 20$), these islands are radially isolated and do not overlap. Thus, they do not satisfy the Chirikov criterion for magnetic stochasticity. Further, assume $L_{\delta B} \simeq 25$ mm. This $L_{\delta B}$ parameter is smaller than but more realistic than the $1/k_\theta \simeq 67$ mm used in [24, 25]. These are the parameters used in determining the field line flutter shown in Fig. 1, except that the magnetic perturbation level there was reduced by a factor of about 3 to $\delta \hat{B}_\rho / B_0 = 10^{-4}$ for visualization purposes.

Results. The $\chi_{e\text{eff}}^{\text{flutt}}$ and $\chi_{eW\text{eff}}^{\text{flutt}}$ electron thermal diffusivities estimated analytically by adding their 10/3 and 11/3 contributions in the $0 \leq X \leq 20$ region between these rational surfaces are shown in Fig. 2. The T_e profiles they predict are shown in Fig. 3. While large χ_e^{flutt} values at rational surfaces flatten the T_e profile there, the average gradient of the T_e profile (dotted line in Fig. 3) is determined predominantly by (see the dotted line in Fig. 2) the minimum thermal diffusivity midway between the surfaces.

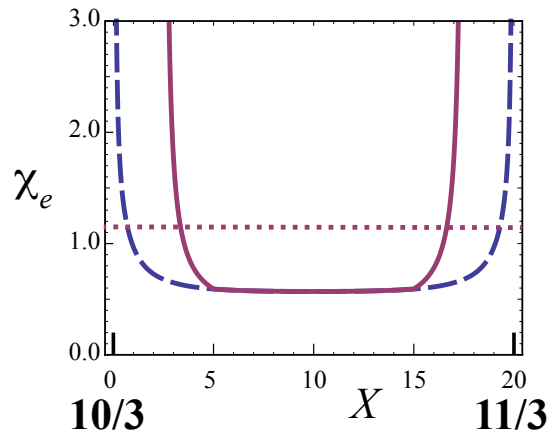


Figure 2. Radial variation of χ_e^{flutt} between the 10/3 and 11/3 rational surfaces without (dashed) and with (solid) islands ($X \equiv x/\delta_{\parallel t}$). The dotted line shows the radially-averaged $\bar{\chi}_e^{\text{flutt}}$ that produces the T_e difference with islands between these rational surfaces which is shown in Fig. 3.

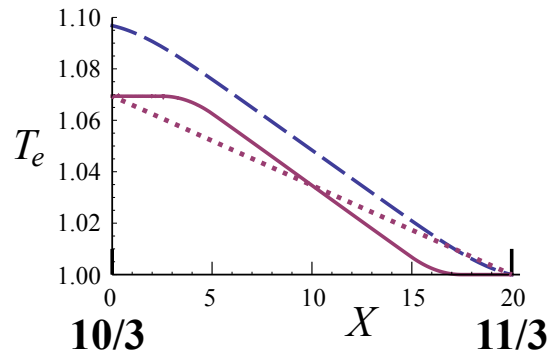


Figure 3. Corresponding predicted T_e profiles between the 10/3 and 11/3 rational surfaces without (dashed) and with (solid) islands. The dotted line shows the T_e profile produced by the $\bar{\chi}_e^{\text{flutt}}$ (dotted line) in Fig. 2.

While the radially-averaged $\bar{\chi}_e^{\text{flutt}} \simeq 1.15 \text{ m}^2 \cdot \text{s}^{-1}$ with magnetic islands determined from the $\Delta T_e / \Delta \rho$ between these surfaces is larger than $\chi_{e \text{ exp}}^{\text{sym}} \simeq 0.6 \text{ m}^2 \cdot \text{s}^{-1}$, it is smaller than the experimentally-inferred [24] $\chi_{e \text{ exp}}^{\text{RMP}} \sim 4 \text{ m}^2 \cdot \text{s}^{-1}$.

Interpretation of results. Since the $\chi_{e \text{ eff}}^{m/n}$ in (16) results from the flutter ambipolar constraint in (15), it probably represents a minimum estimate for $\chi_e^{m/n}$. Conversely, since the magnetic island effects formula $\chi_{e \text{ W eff}}^{m/n}$ in (18) uses the simple linear transition region function F_W and finite perpendicular electron heat transport causes the T_e profile to be smoothed in the island separatrix region (see [46] and discussion in section 3 of [24]), it probably represents a maximum estimate. Thus, the best estimate for the flutter-induced electron thermal diffusivity and T_e profile probably lies between these two estimates. Midway between rational surfaces [i.e., at $|x_{\text{mid}}| \simeq 1/(2nq')$] the low collisionality toroidal model [25] m/n flutter-induced thermal diffusivity is $\chi_{e \text{ t}}^{m/n}(x_{\text{mid}}) \simeq$

$(4\sqrt{2}/13)(c_K c_t^{3/2}) \nu_e \lambda_e^{1/2} (R_0 q)^{3/2} [(\langle \delta \hat{B}_{\rho m/n}^{\text{pl}} \rangle / B_{t0})^2 (|X|^{3/2} G_{11})]_{x_{\text{mid}}}$, which reduces to approximately $\chi_{\text{et}}^{m/n}(x_{\text{mid}}) \simeq 0.5 \nu_e \lambda_e^{1/2} (R_0 q)^{3/2} [\langle \delta \hat{B}_{\rho m/n}^{\text{pl}}(x_{\text{mid}}) \rangle / B_{t0}]^2$ for the DIII-D pedestal top parameters in [24, 25].

Further numerical evaluations. The predicted $\bar{\chi}_e^{\text{flutt}}$ would be slightly larger if other m/n contributions to χ_e^{flutt} were included. However, more precise comparisons require numerical evaluations of the $\chi_{e\text{eff}}^{m/n}$ in (16) and $\chi_{eW\text{eff}}^{m/n}$ in (18) using the flow-screened RMP-induced fields obtained from extended MHD codes [17]–[23]. Numerical studies using DIII-D plasma parameter and toroidal rotation profiles plus M3D-C1 calculations of the $m/n = 8/3, 9/3, 10/3, 11/3$ and $12/3$ $\langle \delta \hat{B}_{\rho m/n} \rangle$ profiles have yielded “diffusivity hills” and T_e profile predictions similar to experimental results at the top of DIII-D pedestals which will be reported elsewhere [43].

Radial electric field implied by flutter ambipolarity constraint. Requiring the flutter-induced electron density flux in (14) to vanish provides a prediction for this electron transport root radial electric field $\mathbf{E}_0 \equiv -\nabla\Phi_0 = -\nabla\rho d\Phi_0/d\rho = \nabla\rho E_\rho$:

$$E_\rho^{\text{flutt}} \equiv -\frac{d\Phi_0^{\text{flutt}}}{d\rho} = -\frac{T_e}{e} \left(\frac{d \ln p_e}{d\rho} + \frac{D_T}{D_{\text{et}}} \frac{d \ln T_e}{d\rho} \right). \quad (22)$$

At the pedestal top, outside narrow layers around the rational surfaces (i.e., for $|x| > \delta_{\parallel t} \simeq 1.5$ mm, $|X| > 1$ [25]) $D_T/D_{\text{et}} \simeq -3/2$. Using this limit in (22) yields a prediction that is qualitatively consistent with RMP ELM-suppressed DIII-D data [47, 48] which indicates a radial electric field $E_\rho \equiv -d\Phi_0/d\rho \sim 10$ kV/m that is negative for $\Psi_N \gtrsim 0.93$ but positive for $\Psi_N \lesssim 0.93$.

5. Effects of non-ambipolar RMP-induced density transport

Non-ambipolar fluxes induced by RMPs. The pedestal top estimates in the preceding section assumed the non-ambipolar radial density fluxes were due solely to the flutter-induced electron density flux $\Gamma_{\text{et}}^{\text{flutt}}$. The corresponding flutter-induced ion density flux would be a factor of $(\nu_i v_{Ti} / \nu_e v_{Te})^{1/2} \sim (m_e/m_i)^{1/2} \sim 1/60$ smaller and hence is negligible. In addition, in the near-separatrix region (e.g., for $\Psi_N > 0.97$) RMPs produce connections of magnetic field lines to divertor plates [6, 8, 23] and thus direct electron losses there [26, 27]. Both of these RMP effects induce a non-ambipolar radial current $J_\rho^{\text{RMP}} < 0$ and thus cause the radial electric field E_ρ to increase to maintain quasineutrality in the edge plasma. RMPs can also induce non-ambipolar ion density fluxes due to additional ion “banana” orbit losses across the separatrix, changes in edge charge-exchange losses and microturbulence-induced transport etc. However, most importantly, the extant non-ambipolar ion density transport is increased by the increase in E_ρ the RMPs induce — to preserve quasineutrality in the plasma.

Electron density flux induced by RMPs. The non-ambipolar electron density flux caused by magnetic flutter in the pedestal region given by the first line of the matrix equation (6) can be written as

$$\Gamma_e^{\text{flutt}}(E_\rho) = -n_e D_{\text{et}} (e/T_e) (E_\rho - E_\rho^{\text{flutt}}). \quad (23)$$

In general, an “offset” radial electric field E_ρ^{offset} (electron transport root) for either stochastic or flutter-driven non-ambipolar electron density transport can be written in the commonly used form [14]:

$$E_\rho^{\text{offset}} = -\frac{T_e}{e} \left(\frac{d \ln n_e}{d\rho} + \hat{\alpha} \frac{d \ln T_e}{d\rho} \right). \quad (24)$$

For stochastic magnetic fields in a sheared slab magnetic field model [49, 14] $\hat{\alpha}$ ranges from $\hat{\alpha}_{\nu=0}^{\text{st}} = 1/2$ for collisionless regimes to $\hat{\alpha}_\nu^{\text{st}} = 1.71$ for collisional regimes in purely hydrogenic ion plasmas (i.e., $Z_i = 1$ with no impurities). However, between rational surfaces at the top of low collisionality pedestals it is likely flow-screening causes magnetic flutter transport to be larger than stochasticity-induced transport. Also the magnetic geometry details (large inverse aspect ratio, near divertor separatrix) and low collisionality regime of electrons become important there [25]. In this situation only untrapped electrons carry the parallel electron heat flow and they have a reduced effective collision length $\lambda_{e\text{eff}}^{\text{ut}} \simeq \lambda_e f_c B_{\text{max}}/B_{\text{t0}}$ ($\sim \lambda_e/3$ for the parameters in [24, 25]). These kinetic-based effects reduce the parallel and consequent flutter-induced radial thermal diffusivities. A collisional limit for $\hat{\alpha}$ is most appropriate near rational surfaces and in the near-separatrix region. For the fully toroidal flutter-induced transport model, the numerical coefficient is $\hat{\alpha}^{\text{flutt}} \equiv 1 + D_T/D_{et}$. It is about $-1/2$ for low collisionality transport midway between m/n rational surfaces where $|k'_\parallel x_0| \lambda_{e\text{eff}}^{\text{ut}} \gg 1$ but near rational surfaces where $|k'_\parallel x_0| \lambda_{e\text{eff}}^{\text{ut}} < 1$ its collisional regime value is $5/2$ [25]. Because its collisional limit is obtained by a procedure analogous to how Braginskii collisional closures are obtained, in the presence of impurities that cause $Z_{\text{eff}} \equiv \sum_i n_i Z_i^2/n_e$ to exceed unity this coefficient can be obtained from inversion of the relevant 3×3 electron collisional friction fluid moment matrix [50]:

$$\hat{\alpha}_\nu^{\text{flutt}} = 1 + \frac{5}{9} \frac{(45\sqrt{2}/16) Z_{\text{eff}} + (33/16) Z_{\text{eff}}^2}{1 + (151\sqrt{2}/72) Z_{\text{eff}} + (217/288) Z_{\text{eff}}^2}. \quad (25)$$

This generalized electron thermal force coefficient [30] yields 1.71 for $Z_{\text{eff}} = 1$ [30, 49], about 1.8–2.0 for typical Z_{eff} pedestal values of 1.4–3, and 2.52 for $Z_{\text{eff}} \rightarrow \infty$ (i.e., about the same as the $5/2$ obtained with the Lorentz collision model in Ref. [25]).

Relation of non-ambipolar fluxes to toroidal torques. The radial non-ambipolar ion density flux (or current density) is more difficult to specify in the edge. (The E_ρ -dependent neoclassical-based radial current density proposed in [51] will not be used in this paper because in standard neoclassical transport theory “the cross-field particle fluxes are ambipolar and independent of the radial electric field” [52] — see also [53, 54, 55, 39].) There are many radial non-ambipolar density fluxes in tokamak plasmas [39]. It can be seen from the toroidal ($\mathbf{e}_\zeta \equiv R^2 \nabla \zeta = R \hat{\mathbf{e}}_\zeta$) component of the species s force balance equation in the form $\mathbf{0} = n_s q_s \mathbf{V}_s \times \mathbf{B}_0 + \sum \mathbf{F}$ that force densities \mathbf{F} which have toroidal components induce radial density fluxes: $q_s \mathbf{e}_\zeta \cdot \mathbf{V}_s \times \mathbf{B}_0 = q_s n_s \mathbf{V}_s \cdot \nabla \psi_p = -\mathbf{e}_\zeta \cdot \sum \mathbf{F}$. Thus, a FSA toroidal torque $T_{s\zeta} \equiv \langle \mathbf{e}_\zeta \cdot \mathbf{F}_s \rangle = \langle R \hat{\mathbf{e}}_\zeta \cdot \mathbf{F}_s \rangle$ induces a FSA radial density flux $\Gamma_s \equiv \langle n_s \mathbf{V}_s \cdot \nabla \psi_p \rangle = \langle \Gamma_s \cdot \nabla \rho \rangle \psi'_p = -T_{s\zeta}/q_s$ in which $\psi'_p \equiv d\psi_p(\rho)/d\rho = RB_p$. Electron and ion torques that are equal in magnitude

but opposite in sign, such as is the case for dynamical friction due to collisions and neoclassical processes [52, 53, 54, 39], produce no radial current in the plasma and hence intrinsically ambipolar fluxes. Unequal electron and ion torques per unit charge produce non-ambipolar density fluxes. The radial electric field is related to the plasma flows (rotation frequencies) via an equilibrium radial force balance equation in the ion form $\Omega_t = E_\rho/\psi'_p - \Omega_{*i} + \Omega_p$ in which Ω_t and Ω_p are the plasma toroidal and poloidal rotation frequencies, and $\Omega_{*i} \equiv (1/n_i q_i) (dp_i/d\psi_p)$ is the toroidal ion diamagnetic flow frequency. Motivated by these theoretical considerations [38, 39], it will be assumed that the dominant FSA non-ambipolar radial density fluxes are linear in E_ρ and can be written phenomenologically in terms of the plasma toroidal torque densities that induce them as

$$\begin{aligned} \Gamma_s^{na} &= -n_s D_s^{na} (q_s/T_s) (E_\rho^{\text{offset}} - E_\rho) \\ &\equiv -\frac{T_s \zeta}{q_s \psi'_p} = m_i n_s \langle R^2 \rangle \frac{\mu_{s\zeta}}{q_s \psi'_p} (\Omega_t - \Omega_s^{\text{offset}}). \end{aligned} \quad (26)$$

Here, D_s^{na} is a non-ambipolar density diffusivity, $E_\rho^{\text{offset}} = (T_s/q_s) d \ln n_s/d\rho + \dots$ is an “offset” electric field, $\mu_{s\zeta} \equiv D_s^{na}/\varrho_{Sp}^2$ is a toroidal rotation damping rate for the species s in which $\varrho_{Sp} \equiv [T_e m_i \langle R^2 \rangle / e^2 \psi_p'^2]^{1/2} = (T_e/m_i)^{1/2} / (e \bar{B}_p/m_i)$ is the ion sound gyroradius in the average poloidal magnetic field $\bar{B}_p \equiv \psi'_p / \langle R^2 \rangle^{1/2}$, and Ω_s^{offset} is an offset frequency. The $D_s^{na} (q_s/T_s) E_\rho$ term in the first line of (26) represents the electric-field-driven “mobility” flux. The flutter-induced density flux in (23) is already in the format suggested by (26). Note also that for the usual case where $E_\rho < E_\rho^{\text{offset}}$ this flutter-induced non-ambipolar electron flux is outward and is caused by the co-current ($\psi'_p > 0$) toroidal torque [25] induced by the flutter-induced Maxwell stress $\langle \mathbf{e}_\zeta \cdot \delta \mathbf{J}_\parallel \times \delta \mathbf{B}_\rho \rangle$. The toroidal rotation damping rate for this flutter-induced torque is $\mu_{e\zeta} = D_{et}^{\text{RMP}} / \varrho_{Sp}^2$.

Non-ambipolar ion density flux. Many ion torques [39] coexist in the pedestal — perhaps mainly charge-exchange and the torque induced by a direct banana ion orbit radial loss current near the separatrix, paleoclassical momentum transport in the near-separatrix steep gradient region of the pedestal [56], and momentum transport due to microturbulence-induced Reynolds stress inward of the pedestal top. Since so many processes can be operative simultaneously, in general the overall plasma torque balance [39] should be employed and solved. However, it will be assumed all relevant torques and the non-ambipolar ion density fluxes they induce can be written in the linear form in (26). Thus, a comprehensive “axisymmetric” (superscript sym) non-ambipolar FSA radial ion density flux before RMPs are applied will be written phenomenologically as

$$\Gamma_i^{\text{sym}}(E_\rho) = n_i D_i^{\text{sym}} (Z_i e/T_i) (E_\rho - E_\rho^{\text{sym}}). \quad (27)$$

Here, E_ρ^{sym} is the radial electric field in the pre-RMP near-axisymmetric transport equilibrium. Since it results from setting this non-ambipolar ion flux to zero, it represents an ion transport root for E_ρ . E_ρ^{sym} can be inferred experimentally from the radial force balance for an impurity ion (e.g., carbon) using charge-exchange recombination spectroscopy measurements of the impurity density, temperature, and poloidal and ion toroidal flows before RMPs are applied. In (27) D_i^{sym} is a

phenomenological non-ambipolar ion diffusivity that might be able to be estimated from responses of the edge electric field to changes in the ion torques in the pedestal region. Note that D_i^{sym} is not the same as the ambipolar density diffusivity D inferred from the usual interpretive recycling source and transport analysis of the electron density.

Determining the radial electric field when RMPs are applied. In order to obtain a quasineutral plasma at a given radius ρ , the radial electric field must adjust to the value needed for the radial non-ambipolar electron and ion density fluxes to be equal — so there is no net radial current in the plasma on the transport time scale (and the plasma toroidal torque balance is satisfied [39]). This requirement has been used previously in stellarator [37] and stochasticity-driven [57] transport analyses. When RMPs are applied, the quasineutrality condition $\Gamma_i^{\text{sym}}(E_\rho^{\text{sym}}) = \Gamma_e^{\text{flutt}}(E_\rho^{\text{sym}})$ yields

$$E_\rho^{\text{amb}} = \frac{E_\rho^{\text{sym}} + \kappa E_\rho^{\text{flutt}}}{1 + \kappa}. \quad (28)$$

Here, κ represents the relative strength of the non-ambipolar flutter-induced electron diffusivity compared to that of the ions:

$$\kappa \equiv \frac{T_i}{T_e} \frac{D_{\text{et}}}{D_i^{\text{sym}}} = \frac{E_\rho^{\text{amb}} - E_\rho^{\text{sym}}}{E_\rho^{\text{flutt}} - E_\rho^{\text{amb}}} \propto \delta \hat{B}_\rho^2. \quad (29)$$

This parameter is the inverse of an analogous parameter postulated in Eq. (13) in [57]. If both flutter and stochasticity are induced by RMPs at a given radius ρ , quasineutrality would be obtained via $\Gamma_i^{\text{sym}}(E_\rho^{\text{sym}}) = \Gamma_e^{\text{flutt}}(E_\rho^{\text{sym}}) + \Gamma_e^{\text{st}}(E_\rho^{\text{sym}})$ which yields $E_\rho^{\text{amb}} = (E_\rho^{\text{sym}} + \kappa^{\text{flutt+st}} E_\rho^{\text{flutt+st}})/(1 + \kappa^{\text{flutt+st}})$, $\kappa^{\text{flutt+st}} \equiv (T_i/T_e)(D_{\text{et}} + D_e^{\text{st}})/D_i^{\text{sym}}$ and $E_\rho^{\text{flutt+st}} \equiv -(T_e/e) d \ln n_e/d\rho - (1/e)(dT_e/d\rho)(D_{\text{et}} \hat{\alpha}^{\text{flutt}} + D_e^{\text{st}} \hat{\alpha}^{\text{st}})/(D_{\text{et}} + D_e^{\text{st}}]$ in which the stochastic (superscript st) quantities are defined via (24) and (26). However, in what follows it will be assumed that stochasticity effects are negligible compared to the flutter effects, i.e., $D_e^{\text{st}} \ll D_{\text{et}}$. Hence only the flutter-induced increase in E_ρ and the pedestal plasma transport modifications the increase in E_ρ induces will be determined.

Variation of E_ρ^{amb} with κ . As illustrated schematically in Fig. 4, the electric field required for flutter model ambipolarity, i.e., the ambipolarity root E_ρ^{amb} defined in (28), is determined from its value where the ion and electron non-ambipolar fluxes are equal. In Fig. 1, it has been assumed that, as is typically the case, $E_\rho^{\text{flutt}} > E_\rho^{\text{sym}}$. As indicated, when RMPs are weak ($\kappa \ll 1$) the electric field approaches the ion root E_ρ^{sym} , whereas if they are very strong ($\kappa \gg 1$) it approaches the electron root E_ρ^{flutt} . Physically relevant values of κ are typically intermediate between these two limits and yield intermediate values of the radial electric field needed for ambipolarity. The concomitant change in the plasma toroidal rotation can be determined from the ion radial force balance. If the ion diamagnetic and poloidal rotation frequencies do not change much, its change is $\Delta \Omega_t \simeq (E_\rho^{\text{amb}} - E_\rho^{\text{sym}})/\psi_p' > 0$. These RMP-induced changes are qualitatively consistent with DIII-D data in ELM-suppressed discharges [4, 26, 47, 48].

Effective flutter-induced diffusivities. The flutter-induced electron density and heat fluxes can be written in terms of effective diffusivities: $D_{\text{eff}}^{\text{flutt}}(E_\rho) \equiv \Gamma_{\text{et}}^{\text{flutt}}(E_\rho)/(-d \ln n_e/d\rho)$ and $\chi_{\text{eff}}^{\text{flutt}}(E_\rho) \equiv \Upsilon_{\text{et}}^{\text{flutt}}(E_\rho)/(-d \ln T_e/d\rho)$. When these fluxes

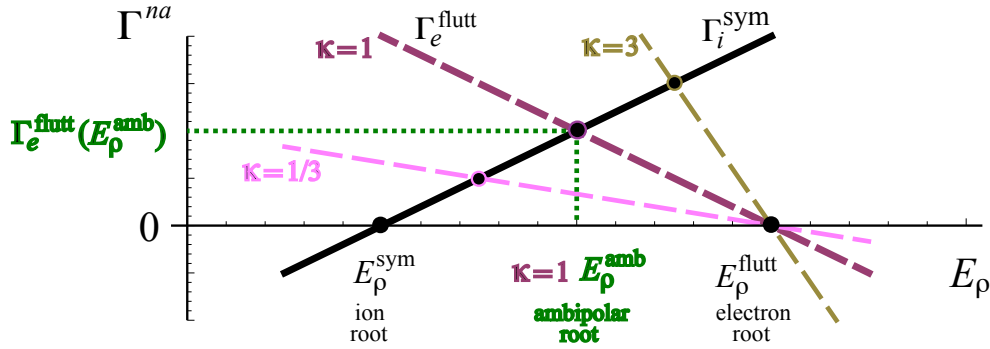


Figure 4. Dependence of the electron and ion non-ambipolar density fluxes on the radial electric field. The sensitivity of the electron flux to E_ρ increases with the strength of the RMPs, which is indicated here by different values of the parameter $\kappa \propto \delta \hat{B}_\rho^2$. The dotted lines indicate the electric field required for ambipolarity and resultant ambipolar density flux for a situation where $\kappa = 1$.

are evaluated at the ambipolar radial electric field E_ρ^{sym} , the effective flutter diffusivities induced by RMPs are

$$D_{\text{eff}}^{\text{flutt}} = D_{\text{et}} \left[\frac{E_\rho^{\text{flutt}} - E_\rho^{\text{amb}}}{-(T_e/e) d \ln n_e / d\rho} \right], \quad (30)$$

$$\chi_{e\text{eff}}^{\text{flutt}} = \chi_{\text{et}} \left[1 - \frac{\chi_n}{\chi_{\text{et}}} \left(\frac{D_T}{D_{\text{et}}} - \frac{E_\rho^{\text{flutt}} - E_\rho^{\text{amb}}}{-(1/e) dT_e/d\rho} \right) \right]. \quad (31)$$

However, flutter induces both a conductive electron heat flux and a convective electron heat flux since in general $\Gamma_{\text{et}}^{\text{flutt}}(E_\rho^{\text{amb}}) \neq 0$. Thus, the “total” flutter-induced electron thermal diffusivity will be defined as

$$\chi_{e\text{tot}}^{\text{flutt}} \equiv \frac{\Upsilon_{\text{et}}^{\text{flutt}}(E_\rho^{\text{amb}}) + (5/2) T_e \Gamma_{\text{et}}^{\text{flutt}}(E_\rho^{\text{amb}})}{-n_e dT_e/d\rho}. \quad (32)$$

Flutter-induced diffusivities at the pedestal top. As indicated in Figs. 2 and 3, at the pedestal top the most important flutter-induced diffusivities are those midway between rational surfaces. The ratios of the diffusivity matrix coefficients [25] were specified above just after (16). For these coefficient ratios the results in (31) and (32) simplify to

$$\chi_{e\text{eff}}^{\text{flutt}} \simeq \chi_{\text{et}} \left[\frac{4}{13} + \frac{6}{13} \frac{E_\rho^{\text{flutt}} - E_\rho^{\text{amb}}}{(1/e) dT_e/d\rho} \right], \quad (33)$$

$$\chi_{e\text{tot}}^{\text{flutt}} \simeq D_{\text{et}} \left[1 + \frac{E_\rho^{\text{flutt}} - E_\rho^{\text{amb}}}{-(1/e) dT_e/d\rho} \right]. \quad (34)$$

In the extreme limit where flutter-induced non-ambipolar transport is dominant ($\kappa \rightarrow \infty$ so $E_\rho^{\text{amb}} \rightarrow E_\rho^{\text{flutt}}$, the electron root) these formulas yield no ambipolar density transport since $D_{\text{eff}}^{\text{flutt}}(E_\rho^{\text{amb}} \rightarrow E_\rho^{\text{flutt}}) \rightarrow 0$ [really $\mathcal{O}\{(m_e/m_i)^{1/2}\} \ll 1$ when ion flutter transport is included] and the effective flutter-induced electron thermal diffusivity in this limit is $\chi_{e\text{eff}}^{\text{flutt}}(E_\rho^{\text{amb}} \rightarrow E_\rho^{\text{flutt}}) \rightarrow (4/13)\chi_{\text{et}} = D_{\text{et}}$, as indicated in (16). This result has been used in the numerical electron transport studies in [43] by assuming

$1/L_{\hat{p}_e} = -(D_T/D_{et})/L_{T_e} \simeq (3/2)/L_{T_e}$ in which $1/L_{\hat{p}_e} \equiv d \ln p_e / d\rho + eE_\rho / T_e$ and $1/L_{T_e} \equiv d \ln T_e / d\rho$. The ratio of the effective flutter-induced electron total thermal to net ambipolar density diffusivity midway between rational surfaces is

$$\frac{\chi_{e \text{ tot}}^{\text{flutt}}}{D_{\text{eff}}^{\text{flutt}}} \simeq \frac{1}{\eta_e} + \frac{-(T_e/e) d \ln n_e / d\rho}{E_\rho^{\text{flutt}} - E_\rho^{\text{amb}}}, \quad (35)$$

in which $\eta_e \equiv d \ln T_e / d \ln n_e$. Since in typical DIII-D pedestals $1/\eta_e \gtrsim 2$, this prediction is apparently comparable to the $\chi_{e \text{ exp}}^{\text{RMP}} / D_{\text{exp}}^{\text{RMP}} \simeq 3$ inferred from the I-coil current scan data from DIII-D pedestals in which RMPs suppressed ELMs [24].

Net ambipolar radial density transport flux: The total ambipolar density transport flux Γ is the sum of all 8 of the intrinsically-ambipolar fluxes Γ^a [39] plus either the electron or ion non-ambipolar flux evaluated at the E_ρ^{amb} value in (28) which makes them equal:

$$\Gamma = \Gamma^a + \Gamma_e^{\text{flutt}}(E_\rho^{\text{amb}}) = \Gamma^a + \Gamma_i^{\text{sym}}(E_\rho^{\text{amb}}). \quad (36)$$

The intrinsically ambipolar density fluxes Γ^a can depend indirectly on the radial electric field, e.g., via effects of shear in the $\mathbf{E} \times \mathbf{B}$ flow on ITG-type modes, particularly just inside the pedestal top (e.g., for $\rho_N \leq 0.88\text{--}0.92$ [58]). RMPs also change the otherwise nearly axisymmetric magnetic field into a slightly 3D field that alters the local magnetic curvature and magnetic shear, which can modify instability characteristics [59] and hence any fluctuation-induced anomalous transport. Thus, RMP-induced changes in the ambipolar density diffusivity D may not be solely due to flutter-induced transport.

6. Flutter model collisionality regime effects and limits

RMP-induced effects are different at higher collisionality. The initial RMP ELM suppression experiments in DIII-D [1, 60, 61] and the recent similar aspect ratio ASDEX-Upgrade ELM mitigation experiments [62] were performed at higher collisionality at the pedestal top where the electron density was larger by a factor of about two which causes the electron temperature to be smaller by about a factor of two. These changes modify key flutter model parameters as follows. The electron collision frequency is increased by a factor of $4\sqrt{2}$, which causes the collision length λ_e and collisionality parameter X_{crit} to both be reduced by a factor of 8 and the dissipative layer width $\delta_{\parallel t}$ to increase by a factor of 8. While $\chi_{\text{et}}^{m/n}(x_{\text{mid}})$ midway between rational surfaces is similar in magnitude, the much larger $\delta_{\parallel t}$ value (~ 12 mm) causes the flutter-induced $\chi_{\text{et}}^{m/n}$ contributions to begin to overlap radially. Thus, the resonant behavior near rational surfaces exhibited in Figs. 2 and 3 and their possible effects on the q_{95} resonance windows on the RMP-suppression of ELMs should be much less evident. Also, the higher collisionality reduces the pedestal bootstrap current which could reduce the kink-type contributions to the toroidal mode coupling responses in the $\langle \delta \hat{B}_{\rho m/n}^{\text{pl}} \rangle$ profiles inward of the rational surfaces [21, 22, 23]. Finally, in these higher density cases it is less likely RMPs can access the electron transport root because more of the NBI momentum will be deposited in the edge and the charge-exchange momentum loss effects are then typically larger. These

effects cause D_i^{sym} to be larger and hence the relative strength κ of RMP effects to be smaller. These comments also apply to the near-separatrix steep gradient region of the pedestal. They could also be especially relevant in pedestals in the very low aspect ratio NSTX [40] and MAST [63] tokamaks because the electron collisionality is also higher in those cases than it is for the DIII-D pedestal top parameters [24, 25] highlighted here.

Collisionality regime limits of flutter model effects. Only untrapped electrons that are sufficiently collisionless contribute to flutter transport [25] — because their effective collision frequency must be less than the transit frequency for their periodic motion around a flux surface. This criterion depends on the speed (energy) of individual electrons and is embodied in the X_{crit} parameter which provides a lower limit on the second energy integral in (11). A rough criterion for significant flutter transport results from requiring the collisionality parameter X_{crit} to exceed unity — so $\lim_{|X| \gg 1} |X|^{3/2} G_{11}$ does not become too small (see Fig. 1 in [25]). This $X_{\text{crit}} > 1$ low collisionality flutter transport requirement can be written as

$$\lambda_e > \lambda_e^{\text{flutt}} \equiv R_0 q \frac{3\sqrt{\pi}}{2} \frac{B_{\text{max}}}{B_{t0}}. \quad (37)$$

Further, the possible q_{95} resonance effects discussed in the preceding paragraph are possible only if the flutter-induced dissipative layers at adjacent rational surfaces are well separated. Since the distance between the $m \pm 1$ and m rational surfaces is $1/nq'$, this resonance behavior condition requires $1/(2nq') \gg \delta_{\parallel t}$ which can be written as

$$\lambda_e \gg \lambda_e^{\text{res}} \equiv R_0 q \frac{12}{\sqrt{\pi}} \left(1 - \frac{B_{\text{min}}}{B_{\text{max}}}\right)^{1/2} \frac{B_{\text{max}}}{B_{t0}}. \quad (38)$$

Since $\lambda_e^{\text{res}}/\lambda_e^{\text{flutt}} = (8/\pi)\sqrt{1 - B_{\text{min}}/B_{\text{max}}} \gtrsim 1$, these two criteria are similar with the resonance condition in (38) requiring a somewhat larger electron collision length.

Pedestal collisionality criterion for flutter model effects. In experimental studies of pedestals the parameter that is often used to characterize the electron collisionality is based on a small inverse aspect ratio neoclassical theory parameter [64, 8]: $\nu_{\text{ped}}^* \equiv R_0 q_{95} \epsilon^{-3/2}/\lambda_{ee}$. Here, λ_{ee} is the collision length for electron-electron collisions which is related to the electron-ion collision length used in this paper by the relation $\lambda_{ee} = \sqrt{2}Z_{\text{eff}}\lambda_e$. Thus, the slightly more restrictive resonance effects criterion in (37) yields a flutter model pedestal collisionality criterion:

$$\nu_{\text{ped}}^* \equiv \frac{R_0 q_{95}}{\epsilon^{3/2} \lambda_{ee}} \ll \frac{\sqrt{\pi/2} B_{t0}/B_{\text{max}}}{12 \epsilon^{3/2} Z_{\text{eff}} (1 - B_{\text{min}}/B_{\text{max}})^{1/2}}. \quad (39)$$

For the DIII-D pedestal top parameters in [24, 25] this yields the condition $\nu_{\text{ped}}^* < 0.5$. This result indicates the flutter model transport and resonance effects should apply to the low collisionality pedestal regime $\nu_{\text{ped}}^* \lesssim 0.2$ used in the ITER-relevant DIII-D [4] pedestals in which RMPs suppress ELMs in limited q_{95} windows [7, 8]. In contrast, the flutter model probably does not apply to the higher collisionality ASDEX-U RMP experiments [62] in which only ELM mitigation is observed. For NSTX pedestals [40] using parameters $\epsilon \simeq 0.59/0.91 \simeq 0.65$, $B_{t0}/B_{\text{max}} \simeq 1/1.65$, $B_{\text{min}}/B_{\text{max}} \simeq 0.35/1.65$

and $Z_{\text{eff}} \simeq 2$, this yields an even lower collisionality condition $\nu_{\text{ped}}^* < 0.1$ — because the collisionality regime of the flutter model is based on untrapped particle physics whereas the neoclassical-based ν_{ped}^* is based on trapped particle physics. Since MAST pedestal parameters [63] are comparable, a similar collisionality condition applies to it as well. Because NSTX [40] and MAST [63] typically operate with $\nu_{\text{ped}}^* > 0.25$ values, the flutter model effects are probably not applicable to the present RMP experiments in very low aspect ratio tokamaks either, where only ELM mitigation is obtained. Thus, the flutter model collisionality criterion in (39) may represent an appropriate criterion for achieving ELM suppression by RMPs in ITER-relevant tokamak pedestals.

7. Summary: Magnetic-flutter-induced transport modifies pedestal structure

Results obtained in this paper. When RMPs are applied to tokamak H-mode plasmas, the flow-screening plasma response in the pedestal region reduces the magnetic perturbations on rational surfaces there and thereby inhibits magnetic stochasticity. However, in the regions between RMP-induced radially isolated chains of magnetic islands at the rational surfaces, the magnetic field lines flutter radially, as described mathematically in (1)–(3) and illustrated in Fig. 1. The electron heat and density transport fluxes induced by this magnetic flutter have been presented previously [24, 25] and are summarized in (6)–(13). This paper develops two frameworks for determining the increases in the radial electric field in the pedestal region caused by the non-ambipolar flutter-induced electron density transport. The first explores the limit where E_ρ is determined by imposing the flutter ambipolarity constraint that the flutter-induced non-ambipolar density flux vanish, as indicated in (14). The consequent electron transport root E_ρ^{flutt} is given in (22) and the resulting reduction in the electron thermal diffusivity in (16). A procedure for including the effects of thin magnetic islands around rational surfaces is proposed in (18). Analytic-based effects of RMP-induced magnetic islands and magnetic flutter on the electron thermal diffusivity and T_e profiles are shown in Figs. 2 and 3. Numerical evaluations of these flutter model predictions over the entire pedestal top region using specific DIII-D RMP experimental profiles and concomitant M3D-C1 $\langle \delta \hat{B}_{\rho m/n}^{\text{pl}}(\rho) \rangle$ profiles that are found to agree reasonably well with experimental results will be published separately [43]. Second, for the more typical case where the flutter-induced non-ambipolar transport is not overly dominant, a measure of its relative importance is given by (29). The $E_\rho \rightarrow E_\rho^{\text{amb}}$ required to obtain ambipolar transport in general is given in (28) and the changes this electric field causes on the flutter-induced effective electron density and thermal diffusivities are given in (30)–(32). Also, predictions are given for the ratio of flutter-induced electron thermal to ambipolar density diffusivity in (35) and total ambipolar density flux in (36). While these various flutter model predictions for E_ρ and its effects are qualitatively consistent with many experimental results [4, 26, 47, 48] in low collisionality DIII-D pedestals where ELMs are suppressed, they remain to be tested quantitatively. Modifications of these effects

at higher collisionality are discussed in the preceding section. Also, criteria for the low collisionality regime where the flutter model predictions should be applicable are given in (37)–(39). The developments in this paper highlight the importance of determining the changes in E_ρ and its effects on flow-screening of the RMP fields in the pedestal, and the resultant changes in the density, toroidal momentum and electron heat transport that are induced by the non-ambipolar density transport caused by adding 3D fields to otherwise nearly axisymmetric (2D) tokamak plasmas. The required low collisionality regime in (39) and flutter-induced changes in E_ρ , flow-screening and plasma transport at the pedestal top may all be significant factors determining the conditions under which RMPs can suppress ELMs in ITER-relevant low collisionality H-mode plasmas.

Model validation. The flutter model provides a new paradigm for explaining how RMPs can increase plasma transport at the top of low collisionality H-mode pedestals. This can cause a diffusivity hill [43] and reduce the electron pressure gradient there, thereby limiting the inward expansion [9, 10] of the pedestal and stabilizing peeling-ballooning instabilities to suppress ELMs. The relative roles of the flutter-induced plasma transport in the top of the pedestal discussed in this paper and the possible effects of an enhanced transport region due to a specific (e.g., 10/3 [9, 10]) magnetic island slightly inward of the pedestal top in limiting inward expansion of the pedestal top and thus preventing ELMs remain to be clarified. This paper has provided new frameworks for evaluating E_ρ and magnetic island effects within the flutter transport model. Also a new framework has been proposed for exploring the increase in the radial electric field caused by the non-ambipolar magnetic-flutter-induced electron density transport. And the effects this increase in E_ρ has in reducing electron heat transport, but increasing plasma toroidal rotation and ambipolar density transport in the pedestal region have been developed. The next steps in the experimental validation of the flutter model of RMP-induced effects on H-mode pedestals are to: 1) test the model over a wider range of parameters, particularly in ν_{ped}^* , 2) quantitatively explore the E_ρ effects on the pedestal parameters, structure, dependences on q_{95} and collisionality, and 3) possibly use the flutter model to explore density pump-out near the separatrix.

Acknowledgments

The authors are grateful to T.E. Evans and R.A. Moyer for discussions of many RMP effects, to S. Mordijck for discussions about her density transport, toroidal rotation and E_ρ analyses [26, 27], to N.M. Ferraro for discussions about his flow-screening M3D-C1 calculations [21, 23], and to P.T. Raum and S.P. Smith for stimulating development of the off-diagonal and magnetic island effects for numerical transport modeling comparisons with DIII-D data [43]. This paper is a significantly expanded version of paper TH/P4-20 presented at the 24th International Atomic Energy Agency Fusion Energy Conference, 8–13 October 2012 in San Diego, CA. This research was supported by US DoE grants DE-FG02-86ER53218 and DE-FG02-92ER54139.

References

- [1] Evans T.E. *et al* 2004 *Phys. Rev. Lett.* **92** 235003
- [2] Evans T.E. *et al* 2006 *Nature Phys.* **2** 419
- [3] Evans T.E. *et al* 2006 *Phys. Plasmas* **13** 056121
- [4] Evans T.E. *et al* 2008 *Nucl. Fusion* **48** 024002
- [5] Fenstermacher M.E. *et al* 2008 *Phys. Plasmas* **15** 056122
- [6] Schmitz O. *et al* 2008 *Plasma Phys. and Control. Fus.* **50** 124029
- [7] Schmitz O. *et al* 2009 *Phys. Rev. Lett.* **103** 165005
- [8] Schmitz O. *et al* 2012 *Nucl. Fusion* **52** 043005
- [9] Snyder P.B. *et al* 2012 *Phys. Plasmas* **19** 056115
- [10] Wade M.R. *et al* 2012 Advances in the Physics Understanding of ELM Suppression Using Resonant Magnetic Perturbations in DIII-D, paper EX/3-1 at 8–13 October 2012 San Diego IAEA FEC
- [11] Tokar M.Z., Evans T.E., Gupta A., Singh R., Kaw P., and Wolf R.C. 2007 *Phys. Rev. Lett.* **98** 095001
- [12] Joseph I. *et al* 2008 *Nucl. Fusion* **48** 045009
- [13] Tokar M.Z., Evans T.E., Singh R., and Unterberg B. 2008 *Phys. Plasmas* **15** 072515
- [14] Kaveeva E., Rozhansky V. and Tendler M. 2008 *Nucl. Fusion* **48** 075003
- [15] Rozhansky V., Kaveeva E., Molchanov P., Veselova I., Voskoboynikov S., Coster D., Kirk A., Ligo S. and Nardon E. 2010 *Nucl. Fusion* **50** 034005
- [16] Rozhansky V., Molchanov P., Kaveeva E., Voskoboynikov S., Kirk A., Nardon E., Coster D. and Tendler M. 2011 *Nucl. Fusion* **51** 083009
- [17] Heyn M.F. *et al* 2008 *Nucl. Fusion* **48** 024005
- [18] Liu Y., Kirk A. and Nardon E. 2010 *Phys. Plasmas* **17** 122502
- [19] Chu M.S. *et al* 2011 *Nucl. Fusion* **51** 073036
- [20] Becoulet M. *et al* 2012 *Nucl. Fusion* **52** 054003
- [21] Ferraro N.M. 2012 *Phys. Plasmas* **19** 056105
- [22] Bécoulet M. *et al* 2012 Non-linear MHD Modelling of Rotating Plasma Response to Resonant Magnetic Perturbations, paper TH/2-1 at 8–13 October 2012 San Diego IAEA FEC
- [23] Ferraro N.M. *et al* 2012 *Nucl. Fusion* **53** 073042
- [24] Callen J.D., Cole A.J., Hegna C.C., Mordijck S. and Moyer R.A. 2012 *Nucl. Fusion* **52** 114005
- [25] Callen J.D., Cole A.J., and Hegna C.C. 2012 *Phys. Plasmas* **19** 112505
- [26] Mordijck S. 2011 Particle transport as a result of Resonant Magnetic Perturbations *Ph.D. Thesis* University of California–San Diego
- [27] Mordijck S. *et al* 2012 *Plasma Phys. Control. Fusion* **53** 122001
- [28] Jakubowski M.W. *et al* 2009 *Nucl. Fusion* **49** 095013
- [29] Shafer M.W. *et al* 2012 *Nucl. Fusion* **50** 122001
- [30] Braginskii S.I. 1965 *Reviews of Plasma Physics* Vol. I, ed M.A. Leontovich (New York: Consultants Bureau) p 205
- [31] Callen J.D. 1977 *Phys. Rev. Lett.* **39** 1540
- [32] Cole A.J. and Fitzpatrick R. 2007 *Phys. Plasmas* **13** 032503
- [33] Waelbroeck F., Joseph I., Nardon E., Bécoulet M. and Fitzpatrick R. 2012 *Nucl. Fusion* **52** 074004
- [34] del-Castillo-Negrete D. and Chacón L. 2011 *Phys. Rev. Lett.* **106** 195004
- [35] Rechester A.B. and Rosenbluth M.N. 1978 *Phys. Rev. Lett.* **40** 38
- [36] Callen J.D., Groebner R.J., Osborne T.H., Canik J.M., Owen L.W., Pankin A.Y., Rafiq T., Rognlien T.D. and Stacey W.M. 2010 *Nucl. Fusion* **50** 064004
- [37] Lore J. *et al* 2010 *Phys. Plasmas* **17** 056101
- [38] Callen J.D., Cole A.J. and Hegna C.C. 2009 *Nucl. Fusion* **49** 085021
- [39] Callen J.D., Cole A.J. and Hegna C.C. 2009 *Phys. Plasmas* **16** 082504; 2013 Erratum **20** 069901
- [40] Canik J.M. *et al* 2011 *Phys. Plasmas* **18** 056118
- [41] Callen J.D., Canik J.M. and Smith S.P. 2012 *Phys. Rev. Lett.* **108** 245003

- [42] Smith S.P., Callen J.D., Groebner R.J., Osborne T.H., Leonard A.W., Eldon D., Bray B.D. and the DIII-D Team, 2012 *Nucl. Fusion*, **52** 114016
- [43] Raum P.T., Smith S.P., Callen J.D., Ferraro N.M. and Meneghini O. 2013 Modeling of RMP-flutter-induced transport in DIII-D (to be published).
- [44] Chang Z. and Callen J.D. 1990 *Nucl. Fusion* **30** 219
- [45] Chang Z. *et al* 1994 *Nucl. Fusion* **34** 1309
- [46] Fitzpatrick R. 1995 *Phys. Plasmas* **2** 825
- [47] Moyer R.A. *et al* 2011 Comparison of Plasma Response Models to Measurements in DIII-D RMP H-mode Discharges, poster TP9 3 at 14–18 November 2011 Salt Lake City APS-DPP Meeting
- [48] Moyer R.A. 2012 Plasma Rotation and Radial Electric Field Response to Resonant Magnetic Perturbations in DIII-D, invited oral TI3 6 at 29 October – 2 November 2012 Providence APS-DPP Meeting
- [49] Kaganovich I. and Rozhansky V. 1998 *Phys. Plasmas* **5** 3901
- [50] See pages 7–9 of 2/21/86 lecture in J.D. Callen, “NE 903 (1986), Fluid Moment Approach for Describing Plasmas” course notes available via <http://homepages.cae.wisc.edu/~callen/plasmas>.
- [51] Rozhansky V., Kaveeva E., Voshkoboynikov S., Coster D., Bonnin X. and Schneider R. 2002 *Phys. Plasmas* **9** 3385
- [52] Hirshman S.P. 1978 *Nucl. Fusion* **18** 917
- [53] Hinton F.L. and Hazeltine R.D. 1975 *Rev. Mod. Phys.* **48** 239
- [54] Hirshman S.P. and Sigmar D. 1981 *Nucl. Fusion* **21** 1079
- [55] Rozhansky V. and Tendler M. 1992 *Phys. Fluids B* **4** 1877
- [56] Callen J.D. 2011 Model for pedestal structure, UW-CPTC 11-4R, 7 November 2011 <http://www.cptc.wisc.edu>
- [57] Kaveeva E., Rozhansky V. and Tendler M. 2008 *Nucl. Fusion* **48** 075003
- [58] McKee G.R., Yan Y., Holland C., Buttery R.J., Evans T.E., Moyer R.A., Mordijck S., Nazikian R., Rhodes T.L., Schmitz O., and Wade M.R. 2012 Turbulence and Transport Response to Resonant Magnetic Perturbations in ELM-Suppressed Plasmas on DIII-D, paper EX/P7-06 at 8–13 October 2012 San Diego IAEA FEC
- [59] Bird T.M. and Hegna C.C. 2013 *Nucl. Fusion* **53** 013004
- [60] Moyer R.A. *et al* 2005 *Phys. Plasmas* **12** 056119
- [61] Evans T.E. *et al* 2005 *Nucl. Fusion* **45** 595
- [62] Suttrop W. *et al* 2011 *Plasma Phys. Control. Fusion* **53** 124014
- [63] Kirk A. *et al* 2012 *Nucl. Fusion* **53** 043007
- [64] Loarte A. *et al* 2003 *Plasma Phys. Control. Fusion* **45** 1549